Performance of a Region II Drift Chamber Prototype and Region II Drift Chamber Tracking

L. M. Qin, J. Yun, G. E. Dodge, C. E. Hyde-Wright, A. Klein, S. E. Kuhn
T. D. Pyron, B. A. Raue, K. G. Vansyoc and L. B. Weinstein
(Submitted September 24, 1996)
Department of Physics, Nuclear and Particle Physics Research Facility
Old Dominion University, Norfolk, VA 23529

1 Introduction

The construction of a thirty-six cell Region II drift chamber [1] prototype has been described in Ref. [2]. The performance of the prototype was evaluated using cosmic ray data in a non-magnetic environment. We summarize the tracking results in this note and present approaches to characterize the drift time and drift distance correlation in both non-magnetic and magnetic environments.

In the second section of the note, the experimental setup is briefly described. A practical approach to parameterize and extract the correlation function between the drift time and the distance-of-closest-approach (doca) from a sense wire to a track is presented in the third section. The variables to quantify the drift chamber performance are also defined. In the fourth and fifth parts of the note, the tracking results from cosmic ray data taken using a pre-mixed argon-ethane gas mixture (50/50 by volume) and various helium-ethane mixtures are presented. The effects of the presence of an inhomogeneous magnetic field on the Region II drift chamber tracking are discussed in section six based on the Garfield [3] simulation. A method to characterize the dependence of the drift time and doca correlation function on the magnetic field is introduced for the Region II drift chamber tracking.

2 Experiment

The prototype consists of thirty-six uniform hexagonal cells in six layers. The cell size, from a sense wire to the field wires of the cell, is 1.335 cm. (The average cell sizes of the axial and stereo superlayers of the Region II drift chambers are 1.34 cm and 1.44 cm, respectively.) We measured the distance between every two adjacent wires in the same layer and obtained a standard deviation of 32 μm.

The prototype was instrumented in the same way as the Region II drift chambers. The CEBAF-designed pre-amplifiers were mounted on the signal translator board.

VPI post-amplifiers and NIM discriminators were used instead of CEBAF-designed amplifier and discriminator boards. The potentials on the sense, field and guard wires were set at relative ratios of 2, -1 and 0.7. The ratios were obtained from Garfield to ensure the gains of all six layers are equal.

A two-way gas handling system was built to mix helium and ethane gases. The mixing ratios were estimated using vendor-supplied flow-rate data sheets [4]

Coincidence signals from a pair of scintillators provided triggers to the data acquisition system, starts for TDC modules and gates for ADC modules. The data files were stored on computer disks and analyzed using a modified version of the CEBAF Track program [5].

3 Data Analysis

3.1 Tracking procedure

For each event, we record the time between trigger firing and sense wire signal arrival and the total ionized charge for all sense wires that fire. The measured drift

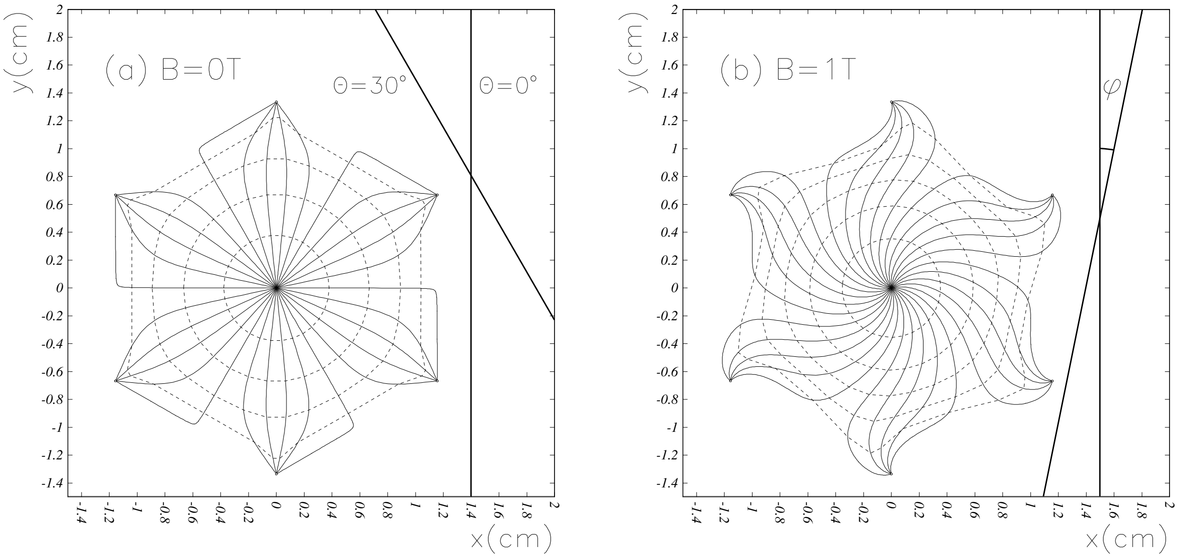

Figure 1: Drift time isochrones (dashed lines) for a hexagonal cell at 2400V for a helium-ethane 50/50 mixture in a (a) zero and a (b) 1 Tesla magnetic field. The separation between two equal time contours is 0.1 μs. The thin solid lines show typical drift paths.

times are then corrected to eliminate passive time delay differences among individual channels. The global time offset is removed by adding a constant to all measured drift times. Distance-of-closed-approaches are calculated from drift times using a correlation function. Eq. 1 is a generic form of the correlation function,

$$x = x(t, \theta, \mathbf{B}), \tag{1}$$

where θ is the entrance angle of a track with respect to a cell which is between 0° and 30° by taking into account the geometrical symmetry without the presence of any magnetic field as shown in fig. 1(a). The effect of the magnetic field $\mathbf{B}$ will be discussed in section six.

The trajectory position is determined by an iterative process using the least squares method. We used a standard method to exclude one of the six layers to study spatial resolutions and efficiencies of the chamber. We started with an initial drift time and doca correlation function from the Garfield simulation. The final distance-of-closed-approaches to sense wires in the excluded layer were calculated and used to optimize the $x(t, \theta)$ function.

3.2 x(t,θ) and maximum drift time

The drift time and doca correlation function is determined by the drift chamber geometry and operational conditions. As pointed out in an earlier CLAS-note [6] and Ref. [7], the maximum drift time may play an important role in parameterizing the $x(t, \theta)$ function. We define the maximum drift time, t_{max}, as the drift time from the location of a field wire to the sense wire of a cell. The electrical field distribution results in the hexagonal equal drift time contour at the edge of a cell as shown in fig. 1(a), which can be described by

$$x(t = t_{max}, \theta) = S\cos(30^\circ - \theta), \tag{2}$$

where S represents the cell size.

We use a simple fourth order polynomial of a reduced drift time $\hat{t}$,

$$x_0(\hat{t}, \theta_0) = a + b\hat{t} + c\hat{t}^2 + d\hat{t}^3 + e\hat{t}^4, \tag{3}$$

to parameterize the correlation function empirically for a particular track entrance angle θ_0. The reduced drift time $\hat{t}$ is defined as $\hat{t} = t/t_{max}$. The use of $\hat{t}$ instead of the drift time t can reduce if not remove the dependences of the coefficients on the absolute maximum drift time. Only four out of the five coefficients in eq. 3 are free parameters and we have from eq. 2

$$e = S\cos(30^\circ - \theta_0) - a - b - c - d. \tag{4}$$

The correlation function for any other angles between 0° and 30° can be obtained from eq. 3 as a leading term plus a small second order correction term,

$$x(\hat{t},\theta) = x_0(\hat{t},\theta_0) + S\left(\cos\left(30^\circ - \theta\right) - \cos\left(30^\circ - \theta_0\right)\right)\alpha(\hat{t}). \tag{5}$$

Our study on differences between the correlation functions of different angles shows the function in eq. 6 is a good approximation for $\alpha(\hat{t})$ in which $\hat{t}_\tau$ is a free parameter.

$$\alpha(\hat{t}) = \hat{t}^2 \exp\left(\frac{\hat{t}-1}{\hat{t}_\tau}\right)^3 \tag{6}$$

We optimize the coefficients of $x_0(\hat{t},\theta_0)$ in eq. 3 by fitting the calculated distance-of-closed-approaches from sense wires in the excluded layer to all reconstructed tracks between 0° and 30°. The angle θ_0 equals the average entrance angle of the data set. The maximum drift time can be obtained by a linear extrapolation from the data points near the cell boundary.

The advantage of this approach is that the $x_0(\hat{t},\theta_0)$ function can be well determined empirically from a limited data set and a limited number of iterations. Since the $x(\hat{t},\theta)$ has a leading term $x_0(\hat{t},\theta_0)$ which reproduces the major features of the correlation function, a reasonably well determined $\hat{t}_\tau$ for the second term in eq. 6 can lead to good tracking results.

We use a total of seven parameters, a, b, c, d, θ_0, $\hat{t}_\tau$ and t_{max} to characterize the correlation function in a non-magnetic environment. A minor change in the operational conditions may not require an update to all the parameters but t_{max} whose change can be monitored [6, 7].

3.3 Spatial resolution and uncertainty of a trajectory

The drift chamber resolution can be extracted from residual distributions obtained from track fitting. A residual is defined as the difference between the predicted doca using the correlation function from a drift time and the calculated doca from the sense wire to the reconstructed track. We estimate standard deviations of the residual distributions by Gaussian fits.

The drift chamber single cell spatial resolution σ_{cell} can be related to the standard deviation σ_{fit} of the residual distribution of single cells in the layers used in track fitting by

$$\sigma_{cell} = \sqrt{N/(N-2)}\,\sigma_{fit}, \tag{7}$$

where N is the number of layers used in the track fitting. (No more than one cell is used for track fitting in each layer.) The standard deviation σ_{ex} of the residual distribution of cells in the excluded layer includes the intrinsic resolution of the drift chamber system and tracking errors. Therefore the uncertainty of the trajectory position at the location of the excluded sense wire layer (one of the two central layers), σ_{track}, can be estimated by

$$\sigma_{track} = \sqrt{\sigma_{ex}^2 - \sigma_{cell}^2}. \tag{8}$$

All uncertainties defined here are measured radially from sense wire positions and are independent of track entrance angles.

4 Argon and Ethane Mixture

We studied the performance of the prototype filled with a pre-mixed 50/50 argon-ethane mixture. We scanned the potential settings on wires at different electronic thresholds set on the sense wire signals. Fig. 2 shows the efficiency plateau for thresholds of 10mv and 40mv.

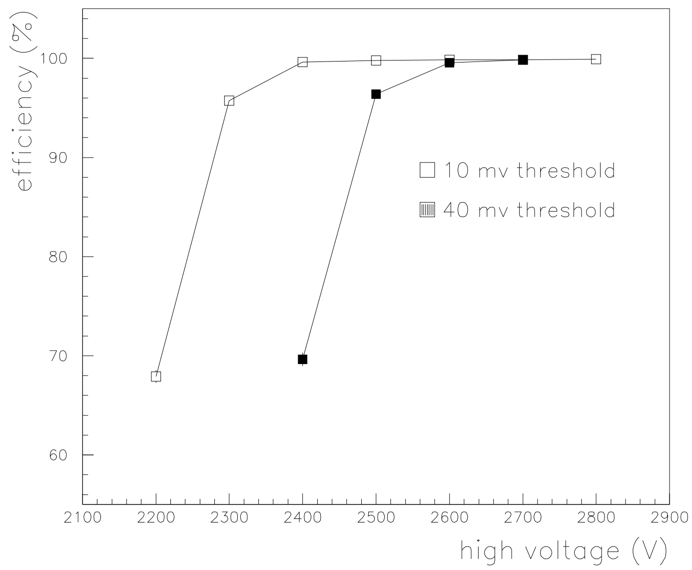

Figure 2: Efficiency plateau for a 50/50 argon-ethane mixture. The high voltage (HV) is the potential difference between sense and field wires.

We optimized the $x(t, \theta)$ correlation function following the procedure described in section three. Fig. 3 is a drift time-doca scatter plot of data taken at 2500V and

10mv threshold, 100V above the plateau starting point. The solid line in the plot is the fitted curve of $x_0(\hat{t}, \theta_0)$ which precisely describes the correlation for small doca where the dependence on the track entrance angle θ is not significant. The second term in eq. 5 serves as a correction to reproduce the dependence at large doca. The dashed lines in the plot show the function at the two angle limits. All the curves have a cut-off at the maximum drift time when they reach the cell boundary. The inset shows the fit to the difference between the doca of $0.25°\pm0.25°$ and $29.0°\pm1.0°$ from which the parameter $\hat{t}_\tau$ is determined.

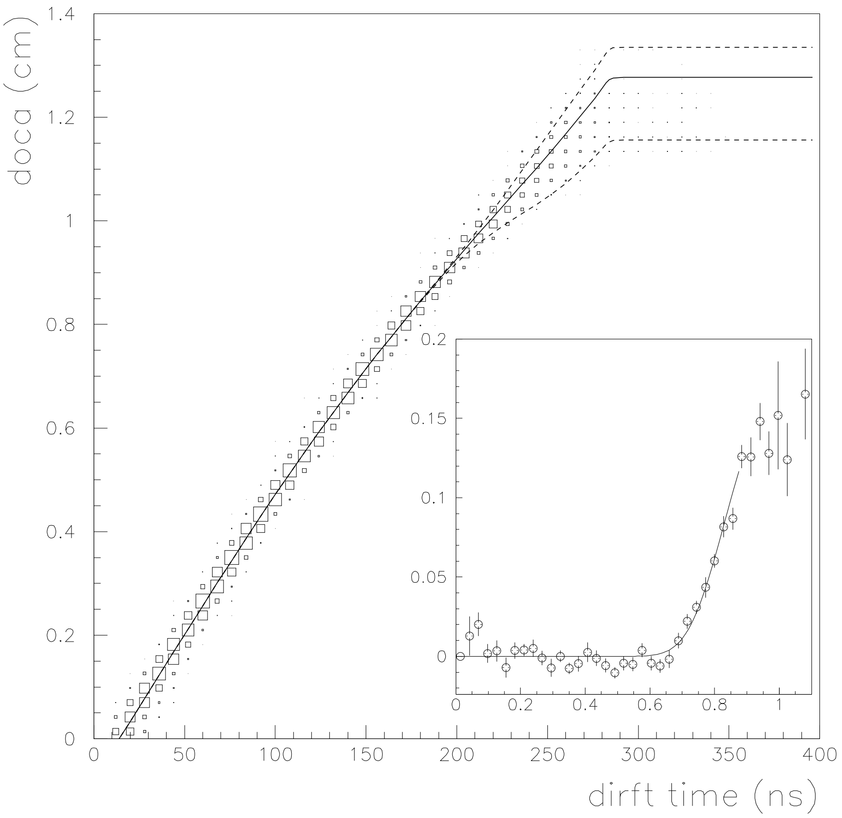

Figure 3: Drift time-doca scatter plot and correlation function for a 50/50 argon-ethane mixture at 2500V and 10mv threshold.

The prototype single cell spatial resolution is plotted in fig. 4 as a function of high voltage. The numerical results and the values of the layer efficiency are listed in tab. 1. A single cell spatial resolution σ_{cell} of better than 150 μm was obtained on the top of the efficiency plateau at 10mv threshold while the track position uncertainty

σ_{track} is better than 100 μm.

HV(V)	efficiency (%)	$\sigma_{fit}(\mu$m)	$\sigma_{cell}(\mu$m)	$\sigma_{ex}(\mu$m)	$\sigma_{track}(\mu$m)
2400	99.6	161	**210**	250	136
2500	99.8	115	**150**	179	98
2600	99.8	96	**125**	157	95
2700	99.8	87	**113**	146	93
2800	99.9	82	**107**	141	91

Table 1: Numerical results of drift chamber resolutions and values of the layer efficiency for a 50/50 argon-ethane mixture at 10mv threshold.

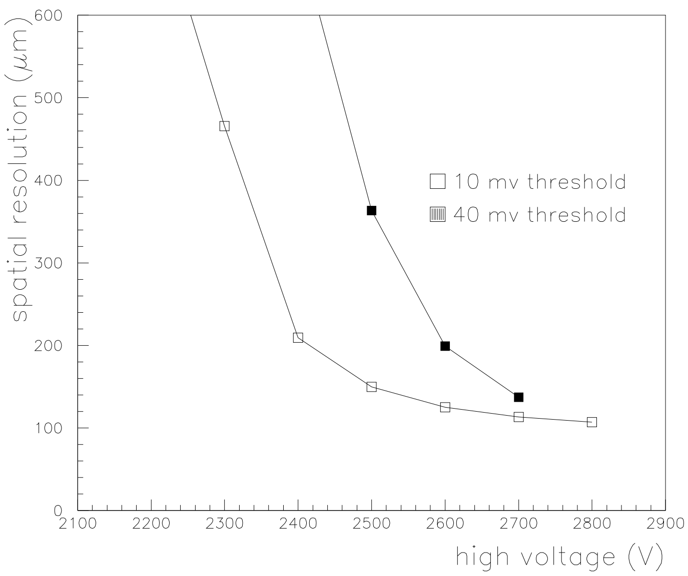

Figure 4: Single cell spatial resolution as a function of HV for a 50/50 argon-ethane mixture.

The drift chamber spatial resolution as a function of doca can be obtained from the residual distribution of cells in the excluded layer. The tracking error σ_{track} was removed from the results shown in fig. 5. The resolution deteriorates near sense wires (small doca) because of the well know statistical fluctuations of primary ionization. The deterioration near the cell boundary (large doca) is mainly a result of the cell geometry, i.e., the field line distribution and low efficiency due to short path length.

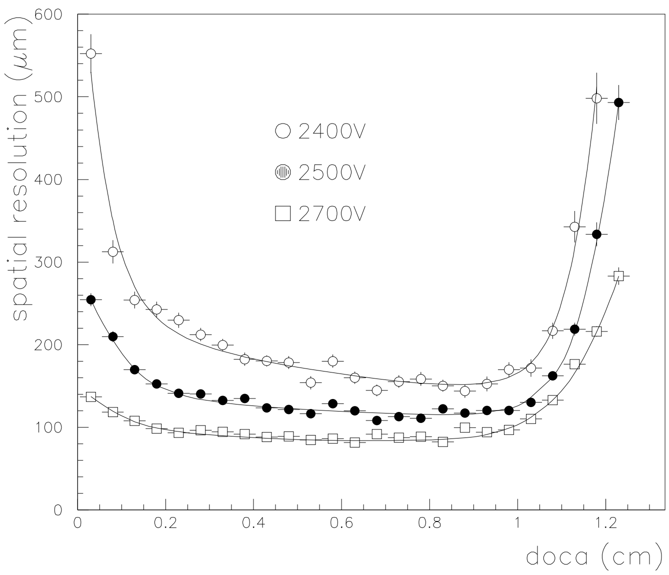

Figure 5: Spatial resolution as a function of doca for a 50/50 argon-ethane mixture at different high voltages and 10mv threshold. The lines serve to guide eyes only.

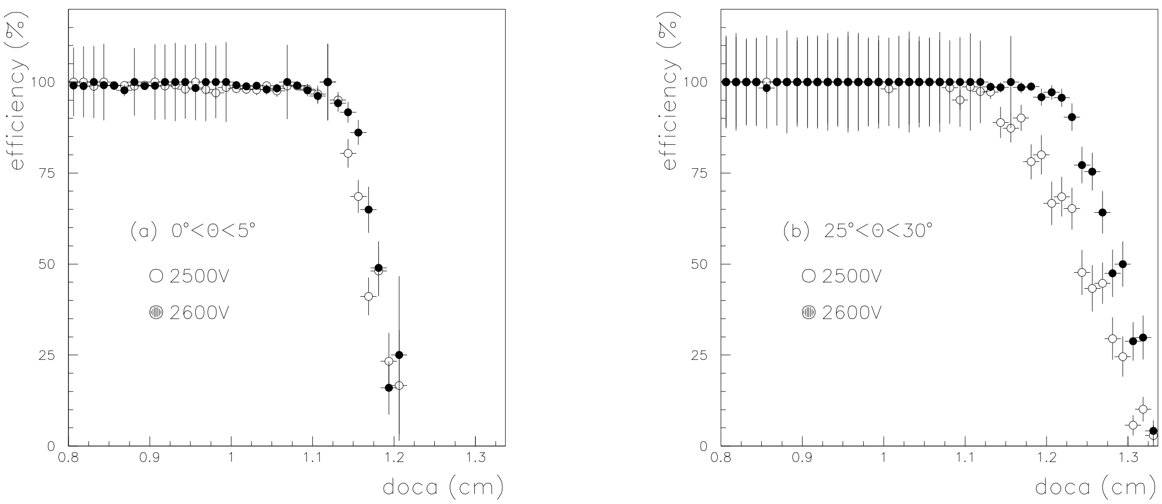

Figure 6: Efficiency as a function of doca for a 50/50 argon-ethane mixture at different high voltages and 10mv threshold for tracks in different angle ranges.

The cell efficiency as a function of doca gradually decreases to zero near the cell boundary except for 0° tracks as shown in fig. 6. There are only slight efficiency improvements for large angle tracks at large doca as the high voltage increases.

We measured the total ionized charges induced by minimum ionizing particles in the active chamber volume. Fig. 7(a) shows the integrated charge distribution of single cells which has a long tail on the higher side, a feature of the Landau distribution. We plot the mean value of the charge distribution as a function of high voltage in fig. 7(b) which is a relative gain measurement for the drift chamber.

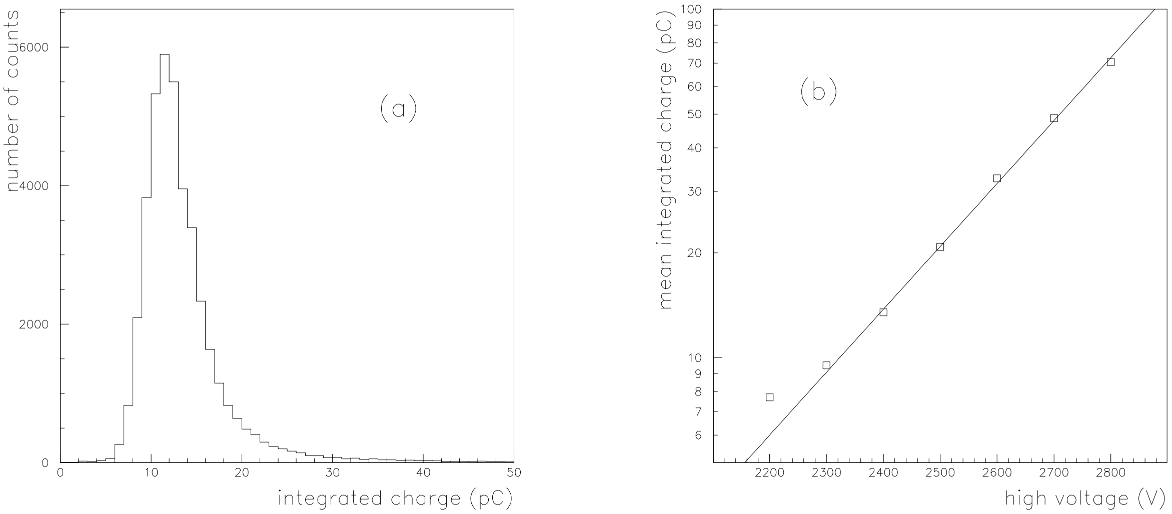

Figure 7: Integrated charge distribution of single cells at 2400V and 10mv threshold (a) and mean value of the distribution as a function of HV (b) for a 50/50 argon-ethane mixture.

5 Helium and Ethane Mixtures

The Region II drift chambers are located in an inhomogeneous magnetic field with a strength up to 2 Tesla [1] which modifies the drift properties of electrons. The use of a helium gas mixture may reduce the impact of the magnetic field on the Region II tracking because the electron-helium collision cross section is larger than that of electron-argon collision [8]. The long radiation length of helium gas can also be of help to minimize multiple scattering in order to improve the CLAS momentum resolution. The typical values of properties of helium, argon, ethane (C_2H_6) gases and their mixtures are summarized from the literature or computed in tab. 2. The radiation length of a 50/50 helium-ethane mixture is about four times as long as that of a 50/50 argon-ethane mixture, which reduces the multiple scattering by a factor of 2.

Gas	Z	A	ρ (g/l)	X_{rad} (m)	dE/dx (keV/cm)	W_i (eV)	n_p (cm^{-1})	n_t (cm^{-1})
He	2	4.003	0.178	5300	0.34	42.3	5.0	8.0
Ar	18	39.95	1.78	109.8	2.69	26.3	24.1	102.3
C_2H_6	18	30.07	1.356	340.35	3.05	24.4	43.6	125.0
Ar/C_2H_6 50/50	18	35.01	1.568	165.7	2.86	25.2	33.8	113.7
He/C_2H_6 50/50	10	17.04	0.767	639.6	1.69	25.4	24.3	66.5
He/C_2H_6 75/25	6	10.52	0.472	1141	1.02	27.3	14.7	37.3

Table 2: Properties of helium, argon and ethane gases and their mixtures: atomic number (Z), atomic weight (A), density (ρ) [9], radiation length (X_{rad}) [9], energy loss (dE/dx) [9], mean energy for ion-electron pair creation (W_i) [10], number of primary ionization (n_p) [10] and total ionization ($n_t=\frac{dE}{dx}/W_i$). The energy loss and numbers of ionization are given at normal condition for minimum ionizing particles.

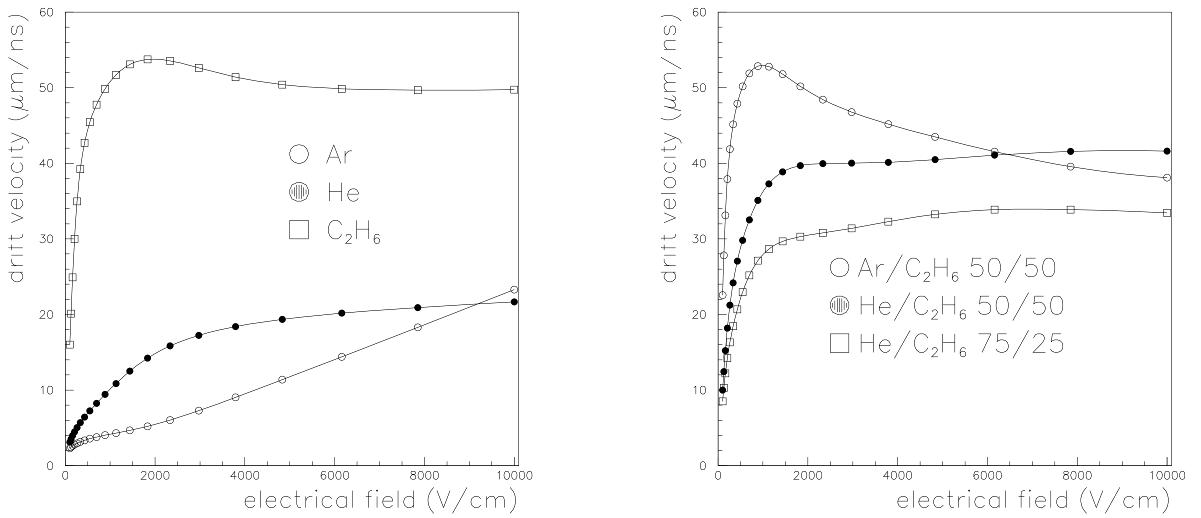

Figure 8: Drift velocity as a function of electrical field for pure helium, argon and ethane gases and their mixtures.

Fig. 8 (a) and (b) show the drift velocity as a function of electrical field for pure helium, argon and ethane gases and their mixtures [3]. The relatively lower drift velocity in a helium-ethane gas mixture results in a longer maximum drift time than in a argon-ethane mixture in a non-magnetic environment. We obtained a maximum drift time of 392 ns in a 50/50 helium-ethane mixture (2700V) and 276 ns in a 50/50 argon-ethane mixture (2500V). The drift time-doca scatter plot of data taken at 2700V and 10mv threshold for the helium-mixture is shown in fig. 9. The curves show the correlation functions as we discussed previously.

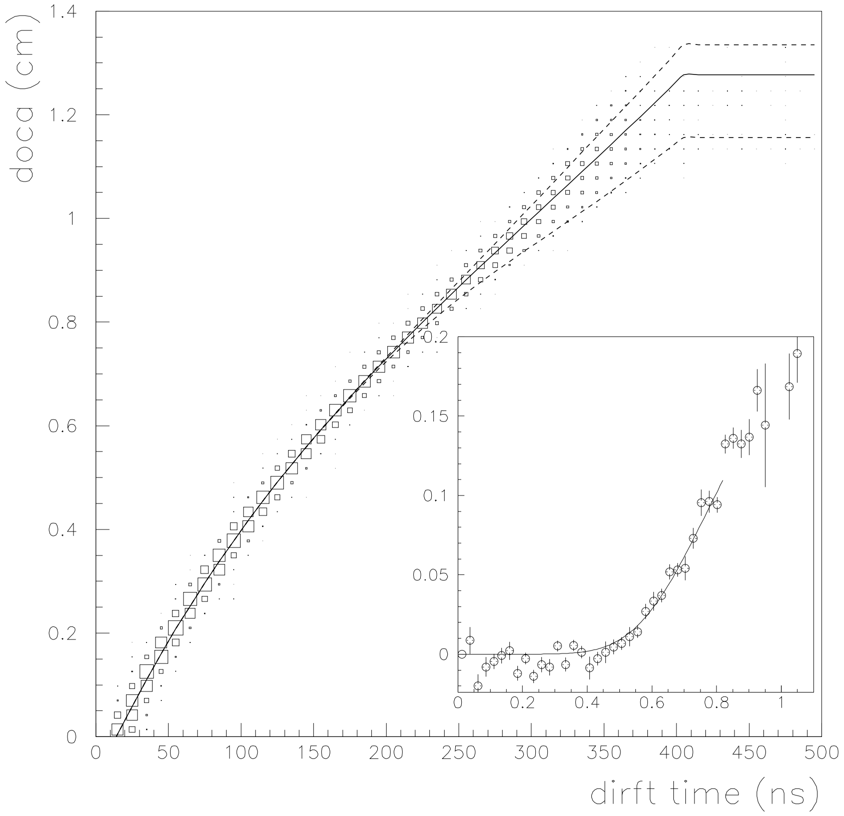

Figure 9: Drift time-doca scatter plot and correlation function for a 50/50 helium-ethane mixture at 2700V and 10mv threshold.

The efficiency plateau for a 50/50 helium-ethane mixture starts at 2600V and 10mv threshold, 200V higher than the 2400V for a 50/50 argon-ethane mixture (fig. 10). The drift chamber single cell resolutions for both gas mixtures are plotted in fig. 11. We found the single cell spatial resolution σ_{cell} better than 140 μm and the track position uncertainty σ_{track} better than 100 μm which are comparable to the results of a 50/50 argon-ethane mixture on the top of the efficiency plateau at the same electronic threshold. The numerical results are listed in tab. 3. The drift chamber resolution as a function of doca is shown in fig. 12 at different high voltages and 10mv threshold. We can see the same features as we discussed for a 50/50 argon-ethane mixture.

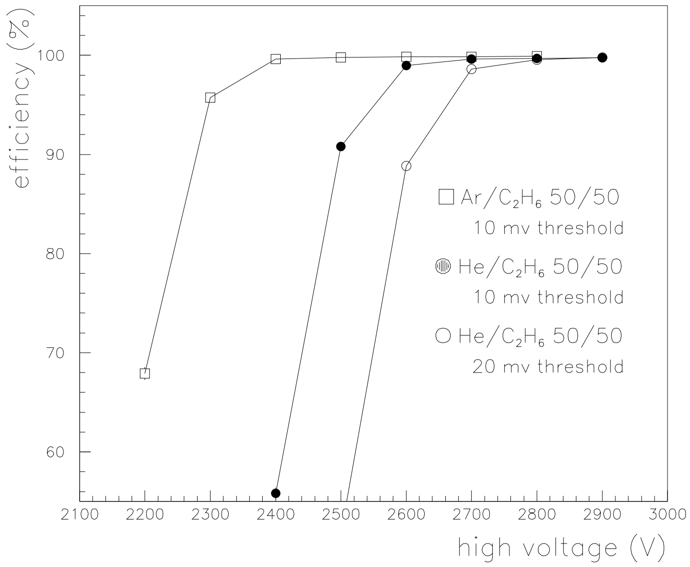

Figure 10: Efficiency plateau for a 50/50 helium-ethane mixture and a 50/50 argon-ethane mixture.

HV(V)	efficiency (%)	$\sigma_{fit}(\mu$m)	$\sigma_{cell}(\mu$m)	$\sigma_{ex}(\mu$m)	$\sigma_{track}(\mu$m)
2600	99.0	139	**182**	216	118
2700	99.6	102	**133**	164	96
2800	99.7	89	**116**	145	88
2900	99.8	82	**106**	138	88

Table 3: Numerical results of drift chamber resolutions and values of the layer efficiency for a 50/50 helium-ethane mixture at 10mv threshold.

A higher percentage of noble gas in a chamber gas mixture yields higher gas gain. We plot the mean value of the charge collected by single sense wires as a

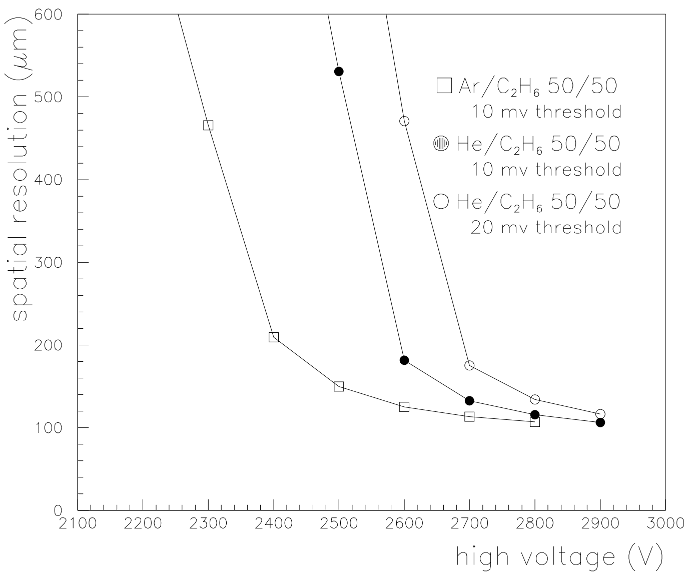

Figure 11: Single cell spatial resolution as a function of HV for a 50/50 helium-ethane mixture and a 50/50 argon-ethane mixture.

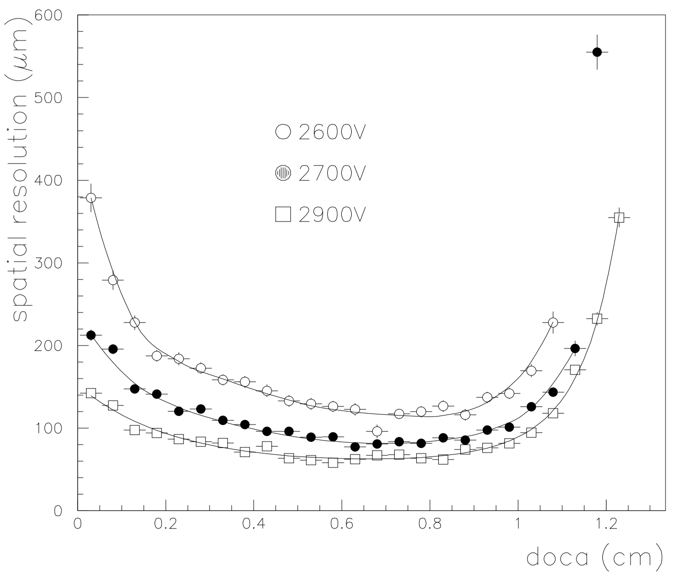

Figure 12: Spatial resolution as a function of doca for a 50/50 helium-ethane mixture at different high voltages and 10mv threshold. The lines serve to guide eyes only.

function of high voltage for different helium-ethane gas mixtures in fig. 13(a). The data were taken using 100-foot-long signal cables instead of 12-foot-long cables used for results presented earlier. The dashed line shows the limit where the efficiency plateau starts.

We have one data point at 2600V and 10mv threshold for a 76/24 helium-ethane mixture which is well on the top of the efficiency plateau. We estimate the efficiency plateau starts at 2260V for the mixture. The spatial resolution σ_{cell} and the track position uncertainty σ_{track} are 143 μm and 111 μm, respectively. We obtained a maximum drift time of 564 ns for the mixture due to the fact that the drift velocity decreases as the percentage of helium increases (see fig. 8). However, the multiple scattering can be further reduced and the impact from a magnetic field is expected to be smaller. Fig. 13(b) shows the gas gain for different helium-ethane mixtures on an arbitrary scale. They are extracted from fig. 13(a) and corrected for the expected energy losses in different gas mixtures. We conclude that we can operate the Region II drift chambers under 2600V using a helium-ethane mixture with the helium percentage (by volume) between 50% and 75% and have a single cell spatial resolution better than 150 μm.

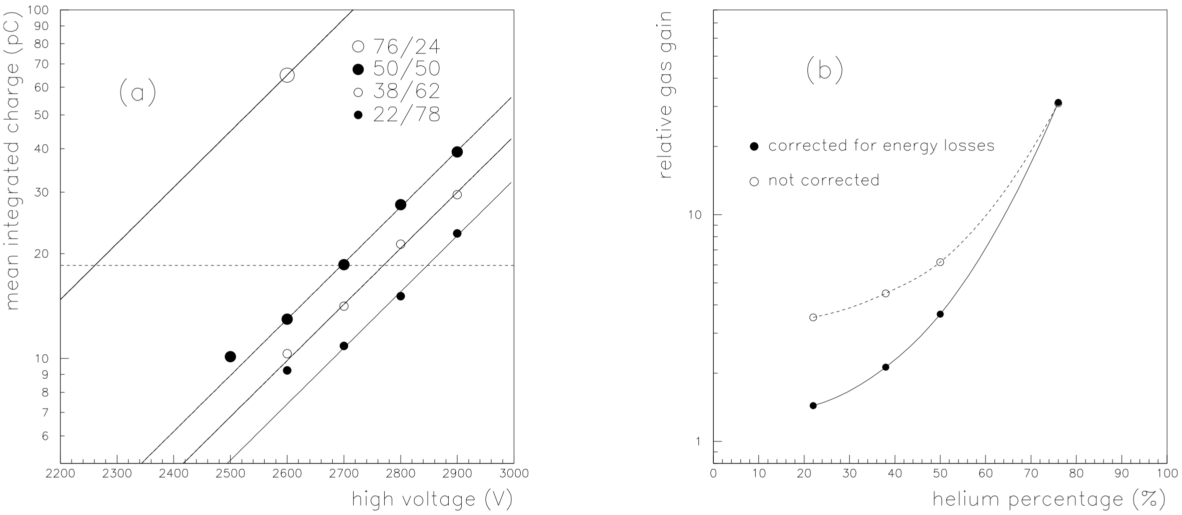

Figure 13: Mean value of the integrated charge distribution as a function of HV (a) and relative gas gain at 2400V for different helium-ethane gas mixtures (b). The dashed line in fig. (a) shows the limit where the efficiency plateau starts. The dashed line in fig. (b) shows the results not corrected for the energy losses.

6 Magnetic Field

The inhomogeneous magnetic field environment of the Region II drift chambers requires an explicit dependence on magnetic field **B** in the drift time-doca correlation function $x(t, \theta, \mathbf{B})$. The Lorentz force causes displacements of drift electrons from electrical field lines and thus prolongs drift paths and times. Fig. 1(b) shows the modified drift lines by a 1 Tesla magnetic field parallel to sense wires. While the hexagonal symmetry is preserved, the equal drift time contour is rotated by an angel φ (clockwise in the x-y plane by a field along positive z axis). We use B to denote the parallel component of a magnetic field in the following text. The rotation angle φ as a function of B is obtained from the Garfield simulation and shown in fig. 14(a).

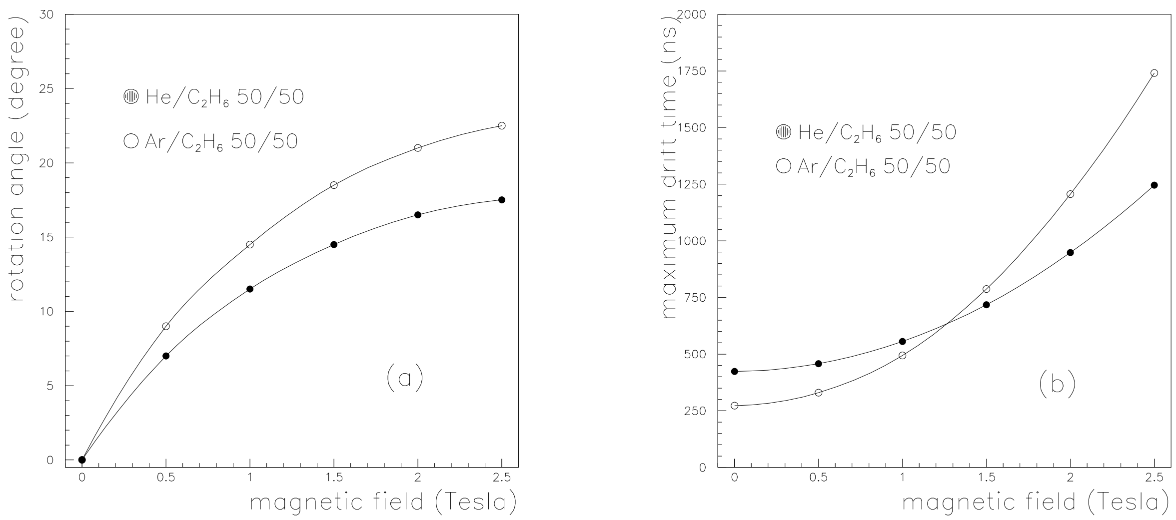

Figure 14: Rotation angle of hexagonal equal drift time contours and maximum drift time as functions of magnetic field for 50/50 helium-ethane and argon-ethane mixtures at 2400V. The solid lines serve to guide eyes only.

The higher electron-atom collision cross section in helium gas [8] results in a shorter mean free path and therefore a smaller magnetic field effect in a helium-ethane mixture than in a argon-ethane mixture. We plot the maximum drift time as a function of B obtained from the Garfield for both 50/50 helium-ethane and argon-ethane mixtures in fig. 14(b). We found a 265% increase of the maximum drift time in the argon-ethane mixture and only a 107% increase in the helium-ethane mixture as the magnetic field B increases from 0.5 Tesla to 2 Tesla.

The presence of a magnetic field not only increases the maximum drift time but also changes the curvature of the drift time-doca correlation function. Fig. 15 shows

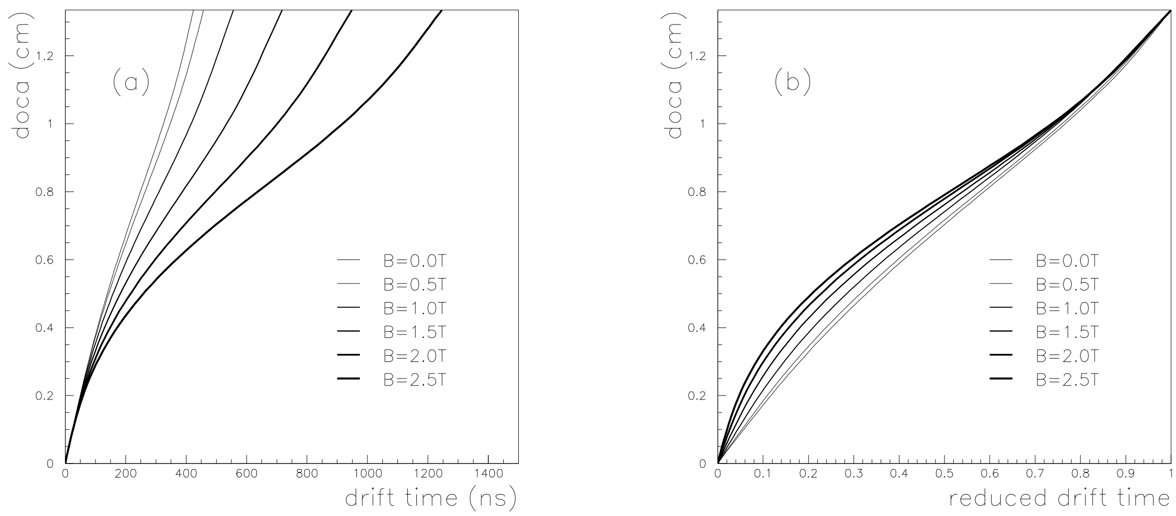

Figure 15: Drift time-doca correlation functions of different magnetic field strengths for a 50/50 helium-ethane mixture at 2400V.

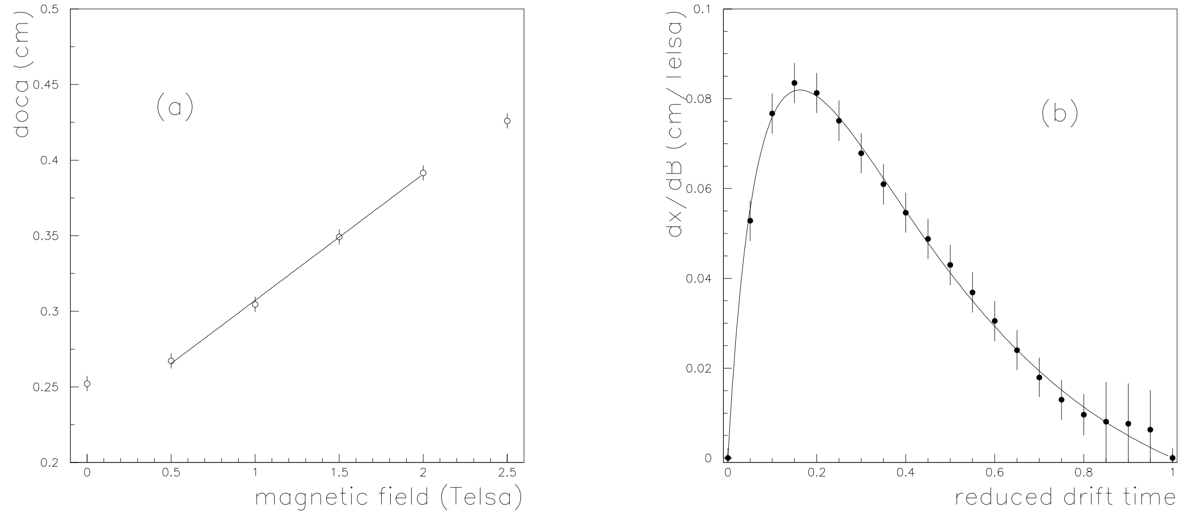

Figure 16: Distance-of-closest-approach as a function of magnetic field B at $\hat{t}$ =0.15 (a) and fit to dx/dB as a function of the reduced drift time (b) for a 50/50 helium-ethane mixture at 2400V.

the correlation functions from the Garfield simulation plotted both as functions of absolute (a) and reduced (b) drift time.

Our simulations revealed a simple linear dependence on the magnetic field B (fig. 16(a)) in a range from 0.5T to 2.0T except at very large doca where the efficiency is low and large distortions on drift paths are expected in a magnetic filed. We introduce an extra correction term to describe the B dependence to $x(\hat{t}, \theta)$ of a particular magnetic field strength B_0,

$$x(\hat{t}, \Theta, B) = x(\hat{t}, \Theta, B_0) + (B - B_0)\beta(\hat{t}). \tag{9}$$

The angle Θ is defined as $\Theta = \theta - \varphi$, which changes the angle limits from 0° and 30° to $-\varphi$ and $30° - \varphi$. We found a good approximation for $\beta(\hat{t})$ in eq. 10 as the result of a fit shown in fig. 16(b).

$$\beta(\hat{t}) = f_B \hat{t}^{1.2}(1 - \hat{t})\exp(-5\hat{t}) \tag{10}$$

We obtained f_B=6.5 which, however, may be considered as a free parameter to be determined from data fitting empirically.

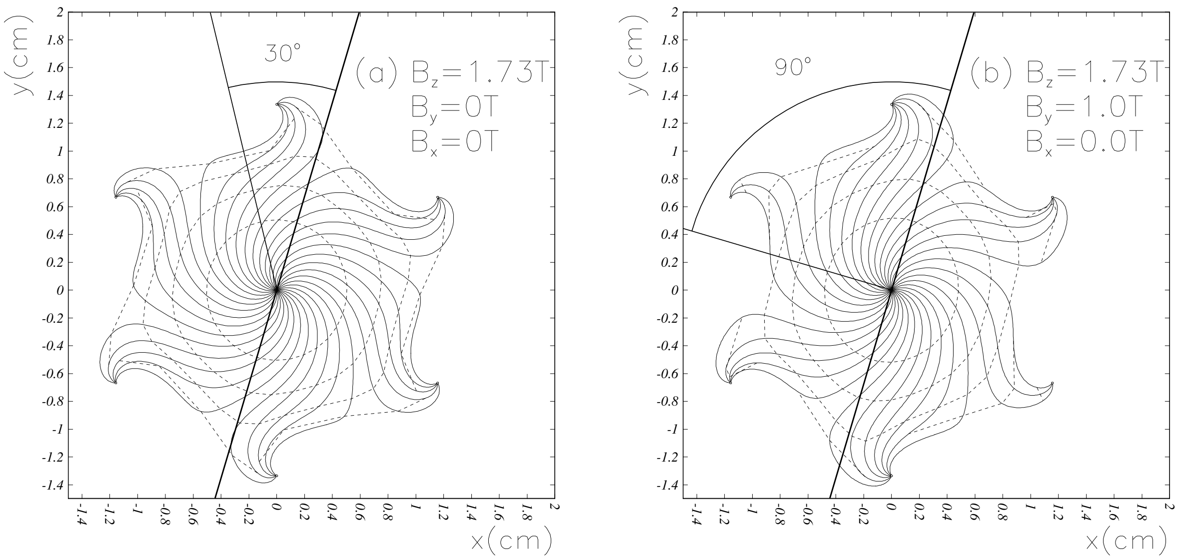

Figure 17: Drift time isochrones (dashed lines) for a hexagonal cell at 2400V for a helium-ethane 50/50 mixture in magnetic fields of 1.73 Tesla parallel (a) and 2 Tesla at 30° with respect to the wires (b). The separation between two equal time contours is 0.2 μs. The thin solid lines show typical drift paths.

The magnetic field component perpendicular to the wires has a less significant impact on the electron drift behavior [11]. However, the presence of such a non-parallel component breaks the hexagonal symmetry as shown in fig. 1(b) and fig. 17(a). The equal drift time contours in a 2 Tesla magnetic field at 30° with respect to the wires in fig.17(b) show a left-right symmetry with respect to the direction of the non-parallel component rotated by the angle φ. (The non-parallel component is parallel to the $\theta = 0°$ tracks in this case.) This symmetry helps to simplify the correction for the effects of a non-parallel magnetic field component. The angle span in which the drift time-doca correlation function needs to be uniquely characterized changes to 90° (fig. 17(b)) from 30° (fig. 17(a)). The detailed dependence of the correlation function on the non-parallel component of a magnetic field $\mathbf{B}$ can be obtained from the Garfield simulation.

We have shown that it is possible to deduce the drift time-doca correlation function for the Region II drift chambers in the inhomogeneous magnetic field of the CLAS from a single polynomial. The maximum drift time, as a parameter, can be used to rescale the correlation function to compensate minor changes in the operational conditions. We can generate a grid for the drift time-doca conversion $x(\mathbf{r}_i, t, \Theta)$ for the Region II drift chamber tracking using the formalism presented in this note on top of the grid for the magnetic field $\mathbf{B}(\mathbf{r}_i)$. We will have a 5×4 matrix for $x(\mathbf{r}_i, t, \Theta)$ at each node of the grid to represent the local correlation function, if we choose the values of doca at five different drift times (0%, 25%, 50%, 75% and 100% of the maximum drift time t_{max}) and four different track entrance angles (0°, 30°, 60° and 90°). The angle of the symmetric axis for the equal drift time contours $\varphi(\mathbf{r}_i)$ can be deduced from the magnetic field at each node. We have a total of 21 quantities at each node in addition to the three components of the magnetic field. However, the computer memory required for the information of the drift time-doca conversion will not be much more than that allocated for the magnetic field since the Region II drift chambers occupy only a fraction of the CLAS field region and require less nodes.

7 Summary

We presented in this note the tracking results obtained from a Region II drift chamber prototype which shows the potential performance of the Region II drift chambers in CLAS. We found single cell spatial resolutions better than 150 μm and track position uncertainties at the center of a superlayer better than 100 μm for both 50/50 helium-ethane and argon-ethane mixtures on the top of the efficiency plateau in a non-magnetic environment.

A helium-ethane mixture with more than 50% helium is a good candidate for the operation of the Region II drift chambers in CLAS. The drift electrons experience less impact from the magnetic field and the multiple scattering is lower than an argon-ethane mixture. The gas gain is high enough to allow the chambers to operate under 2600V with a single cell spatial resolution better than 150 μm.

We introduced a method to parameterize the drift time-doca correlation function based on a fourth order polynomial in which the maximum drift time is utilized. We use two correction terms to describe the geometrical effect and the modification by a parallel magnetic field. An additional correction can be implemented based a left-right symmetry for the non-parallel magnetic field component. The results of this study can be used to develop a scheme of the drift time-doca conversion for the Region II drift chamber tracking in the inhomogeneous magnetic field environment of the CLAS.

References

[1] CEBAF. *Conceptual Design Report - Basic Experimental Equipment*, 1990.

[2] T. D. Pyron. A thirty-six cell prototype for the CLAS Region II drift chamber. *M.S. Thesis, Old Dominion University*, 1996.

[3] R. Veenhof. Garfield, a drift chamber simulation program. *CERN Program Library entry W5050*, 1993.

[4] Matheson Instruments. *166 Keystone drive, Montgomeryville, PA 18936.*

[5] S. Zhou and K. T. Edwards. The CLAS drift chamber track system. *CLAS-NOTE-91-001.*

[6] E. Burtin *et al.* Drift velocity calibration of the CLAS drift chamber. *CLAS-NOTE-95-022.*

[7] M. D. Mestayer *et al.* Construction update and drift velocity calibration for the CLAS drift chamber system. *Nucl. Instr. and Meth.*, **A367**:316, 1995.

[8] W. E. Kauppila and T. S. Stein. Comparisons of positron and electron scattering by gases. *Advances in Atomic, Molecular, and Optical Physics*, **26**:1, 1989.

[9] Particle Data Group. Review of particle properties. *Phys. Rev.*, **D45**:S1, 1989.

[10] W. Blum and L. Rolandi. Particle detection with drift chambers. *Springer-Verlag, second printing*, 1994.

[11] M. Mestayer *et al.* Effects of non-parallel magnetic fields on hexagonal cell drift chambers. *IEEE Trans. on Nucl. Sci.*, **39**:690, 1992.